Translational Oncology
www.transonc.com

Volume 13 Number 1 January 2020 pp. 92–101 92

Predicting Therapeutic Efficacy of Vascular Disrupting Agent CA4P in Rats with Liver Tumors by Hepatobiliary Contrast Agent Mn-DPDP-Enhanced MRI

Yewei Liu[*,†,‡,$], Qiu Guan[‖], Xiangyong Kong[‖], Frederik De Keyzer[†], Yuanbo Feng[†], Feng Chen[†], Jie Yu[†], Jianjun Liu[*,‡], Shaoli Song[*,#], Jos van Pelt[†], Johan Swinnen[†], Guy Bormans[†], Raymond Oyen[†], Shuncong Wang[*,†], Gang Huang[*,‡,$], Yicheng Ni[†,] and Yue Li[*,†]**

[*]Shanghai Key Laboratory of Molecular Imaging, Shanghai University of Medicine and Health Sciences, Shanghai 201318, China; [†]Biomedical Group, Campus Gasthuisberg, KU Leuven, Leuven 3000, Belgium; [‡]Institute of Clinical Nuclear Medicine, Renji Hospital, Shanghai Jiao Tong University School of Medicine, Shanghai 200127, China; [$]Institute of Health Sciences, Shanghai Jiao Tong University School of Medicine (SJTUSM) & Shanghai Institutes for Biological Sciences (SIBS), Chinese Academy of Sciences (CAS), Shanghai 200025, China; [‖]College of Computer Science, Zhejiang University of Technology, Hangzhou 310027, China; [#]Department of Nuclear Medicine, Fudan University Shanghai Cancer Center, Shanghai 200032, China

Abstract

To evaluate hepatobiliary-specific contrast agent (CA) mangafodipir trisodium (Mn-DPDP)—enhanced magnetic resonance imaging (MRI) for predicting the therapeutic efficacy of the vascular disrupting agent combretastatin A4 phosphate (CA4P) in rats with primary and secondary liver tumors, 36 primary hepatocellular carcinomas (HCCs) were raised by diethylnitrosamine gavage in 16 male rats, in 6 of which one rhabdomyosarcomas (R1) was intrahepatically implanted as secondary liver tumors. On a 3.0T MR scanner with a wrist coil, tumors were monitored weekly by T2-/T1-weighted images (T2WI/T1WI) and characterized by Mn-DPDP-enhanced MRI. CA4P-induced intratumoral necrosis was depicted by nonspecific gadoterate meglumine (Gd-DOTA)—enhanced MRI before and 12 h after therapy. Changes of tumor-to-liver contrast ($\Delta T/L$) on Mn-DPDP-enhanced images were analyzed. In vivo MRI findings were verified by postmortem microangiography and histopathology. Rat models of primary HCCs in a full spectrum of differentiation and secondary R1 liver tumors were successfully generated. Mn-DPDP-enhanced $\Delta T/L$ was negatively correlated with HCC differentiation grade ($P < 0.01$). After treatment with CA4P, more extensive tumoral necrosis was found in highly differentiated HCCs than that in moderately and poorly differentiated ones ($P < 0.01$); nearly complete necrosis was induced in secondary liver tumors.

Address all correspondence to: Yue Li, PhD, Shanghai Key Laboratory of Molecular Imaging, Shanghai University of Medicine and Health Sciences, Shanghai 201318, China. E-mail: liy_16@sumhs.edu.cn or Yicheng Ni, MD, PhD, Theragnostic Laboratory, Department of Imaging and Pathology, Biomedical Group, KU Leuven, Herestraat 49, Leuven 3000, Belgium. E-mail: yicheng.ni@kuleuven.be or Gang Huang, MD, PhD, Shanghai Key Laboratory of Molecular Imaging, Shanghai University of Medicine and Health Sciences, Shanghai 201318, China. E-mail: huanggang@sumhs.edu.cn

Received 26 August 2019; Revised 16 September 2019; Accepted 16 September 2019

1936-5233/19
https://doi.org/10.1016/j.tranon.2019.09.010

Mn-DPDP-enhanced MRI may help in imaging diagnosis of primary and secondary liver malignancies of different cellular differentiations and further in predicting CA4P therapeutic efficacy in primary HCCs and intrahepatic metastases.

Translational Oncology (2020) 13, 92–101

Introduction

Liver-specific contrast agents (CAs) for magnetic resonance imaging (MRI) were originally designed to improve the conspicuity of nodular liver lesions based on the presence or absence of hepatocytic uptake and biliary excretion by the lesions of hepatic versus nonhepatic origins [1,2]. Hepatobiliary CAs such as mangafodipir trisodium (Mn-DPDP), gadoxetic acid (Gd-EOB-DTPA), and gadobenate dimeglumine (Gd-BOPTA) have been commercially available and widely used in both clinical [3–5] and animal [6–9] studies to diagnose and differentiate hepatic nodules. In addition to diagnostic imaging, liver-specific CAs could also be explored to guide clinical intervention of hepatic malignancies under real-time MRI monitoring [10].

Being the only non-Gd-based paramagnetic hepatobiliary CA, prolonged enhancement of Mn-DPDP on T1-weighted images (T1WI), especially at a delayed phase (e.g. 24 h), shows superior performance with respect to predicting histological differentiations of hepatocellular carcinomas (HCCs) [11,12] and distinguishing them from secondary liver tumors [13,14]. Specifically, Mn-DPDP leads to positive tumor enhancement for up to a few days among grade I-III differentiated HCCs, but negative enhancement in undifferentiated grade IV HCCs [15]. Secondary liver tumors are discriminated by rim and segmental enhancement at 24 h [13,14]. Despite these merits, commercial Mn-DPDP under the trade name Teslascan was withdrawn from US and EU clinics in 2012 because of unsuccessful marketing and concerns over potential toxicity of free Mn^{+2} ions [16]. However, appeals to revive Mn-DPDP and analogues for clinical and experimental purposes are being proposed [17].

Previously, we have demonstrated that the therapeutic efficacy of a vascular disrupting agent (VDA), combretastatin A4 phosphate (CA4P), on primary HCCs in rats was diverse and negatively correlated with tumor vascularity and cellular differentiation [18]. To facilitate the next initial clinical trials of a dual targeting pan-anticancer strategy namely OncoCiDia [19] among patients with primary HCCs of various differentiation grades, patient selection deems critical to maximize CA4P-induced tumor necrosis, which further serves as a stromal target for the subsequent targeted intratumoral radiotherapy [20]. However, needle biopsy for making histological diagnosis before CA4P therapy is invasive, narrow-viewed, and of complications. Therefore, we hypothesized that Mn-DPDP-enhanced MRI could serve as a virtual biopsy technique to noninvasively map HCCs of diverse cellular differentiations and to further predict those HCCs for their responses to CA4P therapy on the basis of their cellular differentiations.

In this preclinical translational animal experiment, we have studied 1) Mn-DPDP-enhanced MRI to noninvasively characterize primary and secondary liver tumors before therapy; 2) Gd-DOTA-enhanced MRI to indicate in vivo tumor necrosis after CA4P therapy; 3) tumor differentiation and necrosis as verified by postmortem histomorphologic examinations; and 4) correlations between the degree of tumor enhancement by Mn-DPDP-enhanced MRI and the grade of tumor differentiation and the extent of necrosis as indicators for tumoricidal effect of CA4P.

Materials and Methods

Animals and Reagents

Male Wistar Albino Glaxo/Rijswijk (WAG/Rij) rats weighting 250–300 g were purchased from Charles River Breeding Laboratories, Inc. (St. Aubain les Elbeuf, France). The hepatobiliary MRI CA Mn-DPDP (Teslascan; GE Healthcare Nycomed, Norway/Chalfont St. Giles, United Kingdom/Princeton, NJ, USA), nonspecific MRI CA Gd-DOTA (Dotarem; Guerbet, France), oral carcinogen DENA (N0258; Sigma–Aldrich, St. Louis, MO, USA), CA4P (C643025; Toronto, Canada), x-ray CA barium sulfate suspension (Micropaque; Guerbet, France), and gas anesthetic isoflurane (Forane; Baxter Healthcare, Deerfield, IL) were all commercially obtained.

Animal Models of Primary and Secondary Liver Cancer

All animal experiments were approved by the ethics committee of our university KU Leuven in accordance with European and national regulations for animal care and use. In vivo procedures such as gavage feeding, tumor implantation, CA injection, and MRI scanning were performed under gas anesthesia with 2% isoflurane (Harvard Apparatus, Holliston, MA). All rats survived throughout these experimental procedures.

To induce primary HCCs with underlying liver cirrhosis, 16 rats received oral gavage of DENA at 5 mg/kg/day for 14 weeks by using a 16-cm-long flexible plastic esophageal gastric tube (Fuchigami Kikai, Kyoto, Japan) [21]. Tumor growth was monitored weekly by T2-weighted (repetition time, 4000 ms; echo time, 70 ms; flip angle, 150°; field of view, 75 × 56 mm^2; matrix, 256 × 192) turbo spin echo (TSE) images (T2WI) from the 9th week onward. To induce the metastatic liver tumor model as a negative control for absent hepatobiliary CA uptake, 6 rats subjected to laparotomy on the 5th month, and a 1-mm [3] tissue block of rhabdomyosarcoma (R1) was implanted into the lower part of the medium liver lobe, so both the primary and secondary liver malignancies were born in the same liver of the same rat for intraindividual comparisons [22]. Liver tumors were monitored weekly by MRI until the maximum HCC and/or R1 tumor in each rat reached more than 8 mm, respectively.

Contrast-Enhanced MRI With Mn-DPDP and Gd-DOTA

MR images were acquired on a clinical 3.0T whole-body scanner (MAGNETOM Prisma; Siemens, Erlangen, Germany) with a human wrist coil (Hand/Wrist 16, A 3T Tim coil; Siemens). A T1-weighted (repetition time, 626 ms; echo time, 15 ms; flip angle, 160°; field of view, 75 × 56 mm^2; matrix, 256 × 192). TSE

sequence was used for imaging before and after CA administration. Sixteen axial images with a slice thickness of 2.2 mm and a gap of 0.4 mm were acquired.

One week before CA4P therapy, the hepatobiliary-specific CA Mn-DPDP at dose of 0.025 mmol/kg was intravenously injected at a rate of 1 mL/min, after precontrast MR scan was performed. Prolonged Mn-DPDP enhancement was appreciated at 24 h post-contrast, not only to exclude the blood-pool effect resulting from variable tumor vascularity but also to achieve the most distinguished contrast between tumor and liver after the excretion of Mn-DPDP from surrounding liver parenchyma.

Four hours before CA4P treatment, an intravenous bolus of the nonspecific agent Gd-DOTA at 0.2 mmol/kg was injected right before the serial CE-T1WIs were collected.

Qualitative and Quantitative MR Imaging Analyses

MR images were analyzed by 3 coauthors on a built-in software on Siemens workstation (Syngo MR D13D) and MeVisLab (version 2.6.2; MeVis Medical Solutions AG, Bremen, Germany) in a random and blinded fashion.

1) Tumor diameter

On T2WI, tumors were manually delineated on all lesion-containing slices for automatically generating tumor volume by the software, from which the tumor diameter was converted.

2) Change of tumor-to-liver contrast (ΔT/L)

Based on Mn-DPDP-enhanced MRI, hepatomas and surrounding livers were manually contoured with an operator-defined region of interest (ROI) on tumor-containing T1WIs. On tumor-containing slices before and 24 h after contrast, ΔT/L was quantified according to the following formula: $\Delta T/L = postcontrast\ SI_{tumor}/SI_{liver} - precontrast\ SI_{tumor}/SI_{liver}$, where SI stands for signal intensity.

CA4P Therapy

After diagnostic CE-MRI, rats were intravenously injected with CA4P at 10 mg/kg. Gd-DOTA-enhanced MRI was acquired 12 h after therapy to detect in vivo tumor necrosis induced by CA4P.

Digital Microangiography

After the last MRI scanning, rats received laparotomy to infuse hepatic artery with barium suspension before the entire tumor-bearing liver was excised. With a digital mammography unit (Em-brace; Agfa-Gevaert, Mortsel, Belgium), postmortem hepatic arteriography was made at 26 kV and 32 mA to document global tumor vascularity. Then livers were formalin-fixed and sliced into 3-mm sections in the axial plane corresponding to the MR images for being radiographed again at 26 kV and 18 mA to qualitatively validate tumor blood perfusion.

Histopathology

Tissue specimen was paraffin-imbedded, sliced, and stained with hematoxylin and eosin (H&E). An Axiovert 200M microscope equipped with an AxioCam MR monochrome digital camera (Carl Zeiss Inc, Gottingen, Germany) and AxioVision 4.8 software were used for microscopic analyses.

1) Grading of cellular differentiation in HCC

Because of the high analogy to histopathological progression observed in human liver cancer, rat HCCs were diagnosed according to the classical histomorphologic features [23]. The differentiation of rat HCCs was further graded by the World Health Organization Classification [24] as a standard criteria, corresponding to the 4-scale Edmondson and Steiner system [25]: grade I, well-differentiated

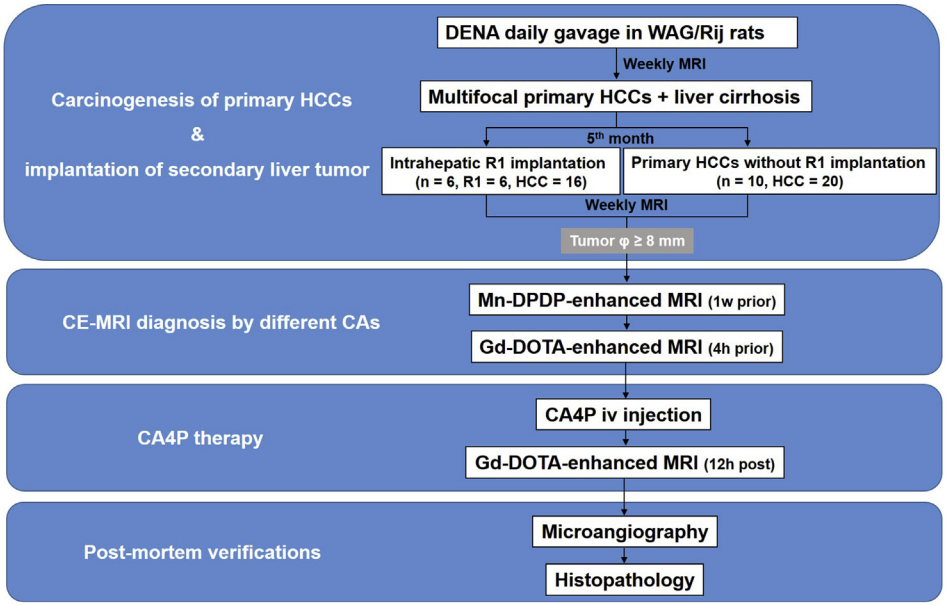

Figure 1. Flowchart of experimental design. WAG/Rij rats: Wistar Albino Glaxo/Rijswijk rats; HCCs: hepatocellular carcinomas; DENA: diethylnitrosamine; MRI: magnetic resonance imaging; R1: rhabdomyosarcoma; n: number of animals; Ø: diameter; CE: contrast-enhanced; CA: contrast agent; Mn-DPDP: mangafodipir trisodium; Gd-DOTA: gadoterate meglumine; w: week; h: hour; CA4P: combretastatin A4 phosphate; iv: intravenous (ly).

HCCs, is composed of tumor cells with minimal atypia in a thin trabecular pattern with 2- to 3-cell palates; grade II, moderately differentiated HCCs, is composed of tumor cells arranged in a trabeculae structure with 4+ cell layers in thickness, having eosinophilic cytoplasm, round nuclei, and prominent nucleoli; grade III, poorly differentiated HCCs, is composed of tumor cells that proliferate in a solid pattern with neoplastic and pleomorphic tumor cells, and with slit-like blood vessels rather than distinct sinusoid-like vasculature; grade IV, undifferentiated HCCs, is characterized by the tumor cells with scant cytoplasm and ovoid/round nuclei, growing in a solid or medullary pattern, in which the type of angioma-like HCCs is also included [6,7].

2) Calculation of CA4P-induced intratumoral necrosis

Digital images of tumor slices at the magnification of 12.5 were used to estimate the percentile tumor necrosis via the ImageJ software [26]. Briefly, ROIs were delineated around the entire tumor and the necrotic tumor, respectively, to obtain "necrotic ratio on each section." For each tumor section, the axial slide in the largest diameter of each tumor block was selected as "section area." Tumor necrosis on H&E-stained slices was estimated independently by 2 pathologists and calculated with the following equation: *Intratumoral necrosis ratio (%)* $= \sum$ *[Necrotic ratio on each section (%)* $\times$ *section area* (mm^2)*]* $\times$ *section thickness (mm)/[4/3*π r^3*]* (mm^3).

Statistical Analyses

Linear regressions were conducted to correlate HCC cellular differentiation with ΔT/L contrast and tumor necrosis ratio. ΔT/L contrast results expressed as the median ± interquartile range were compared both intraindividually and interindividually among primary HCCs of 4 differentiation grades and secondary liver R1 tumor by Kruskal–Wallis test using GraphPad Prism (version 7.02; GraphPad Software Inc, La Jolla, CA, USA). Predictive performance of ΔT/L was analyzed by the receiver operating characteristic (ROC) analysis using MedCalc v. 10.4.8.0 (MedCalc software, Mariakerke, Belgium), in which the areas under the ROC curve were compared to define the cutoff values between various differentiation grades of primary HCCs, as well as between primary and secondary liver tumors, with the maximized sensitivity and specificity. A significant difference was concluded for $P < 0.05$.

Results

Tumor Yield

A total of 36 primary HCCs and 6 implanted R1 tumors were generated in 16 rats of cirrhotic livers (Fig. 1). As summarized in Table 1, primary HCCs were histologically identified in a full spectrum of differentiation including 6 grade I (16.7%), 15 grade II (41.7%), 14 grade III (38.9%), and 1 grade IV (2.8%) lesions; tumor diameter ranged from 6.9 to 22.4 mm. Yet the only one undifferentiated (grade IV) HCC was proven to be an angioma-like HCC [6], which is not solid tumor and rarely exists in human patients. Meanwhile, the secondary R1 liver tumors were all confirmed as nonhepatocyte-derived rhabdomyosarcomas in diameters between 6.7 and 19.5 mm (Table 1).

Mn-DPDP-Enhanced MRI for Diagnostic Imaging of Primary and Secondary Hepatic Nodules

On plain MRI, primary HCCs and secondary R1 tumors appeared hyperintense on T2WI (Figs. 2*A*, 3*A* and 4*A*, 5*A*, 6*A*), and isointense to slightly hyperintense on T1WI (Figs. 2*B*, 3*B* and 4*B*, 5*B*, 6*B*) relative to the surrounding liver. On Mn-DPDP-enhanced images, HCCs were depicted by various degree of positive contrast enhancement at 24 h (Figs. 2*C*, 3*C* and 4*C*, 6*C*). Specifically, well-differentiated HCCs exhibited remarkable tumor enhancement with clear margin (Fig. 2*C*); moderately differentiated HCCs revealed discernible tumor enhancement (Figs. 3*C* and 6*C*); poorly differentiated HCCs (Figs. 4*C* and 6*C*) varied from hyperintense to almost isointense over the liver intensity at 24 h after Mn-DPDP administration.

In comparison with the primary HCCs, secondary intrahepatic R1 tumors often demonstrated marked contrast enhancement in the peritumoral zone at 15 min after Mn-DPDP intravenous injection, which persisted until 24 h without any contrast enhancement in the central bulk of the lesion (Fig. 5*C*).

CA4P Therapeutic Responses Evaluated by Gd-DOTA-Enhanced MRI and Postmortem Analyses

To visualize CA4P-induced tumor necrosis in vivo, Gd-DOTA-enhanced T1WI was performed. Initially, all primary and secondary hepatic tumors were positively enhanced (Figs. 2*D*, 3*D* and 4*D*, 5*D*, 6*D*). Twelve hours after CA4P treatment, massive to nearly complete necrosis was revealed in well-differentiated HCCs (Fig. 2*E*) as well as secondary in R1 liver tumor (Fig. 5*E*), reflected by a nonenhanced central zone surrounded by a brightly enhanced rim at the periphery. In comparison, merely focal necrosis occurred in moderately (Fig. 3*E*) to poorly differentiated (Fig. 4*E*) HCCs, shown as patchy or scattered minute unenhanced foci in largely enhanced masses.

Postmortem microangiography and histological staining helped to verify imaging findings on tumor differentiation and necrosis. Massive tumor necrosis inside well-differentiated HCCs (Fig. 2*J* and *K*) and secondary liver tumors (Fig. 5*J*) was supported by the filling-defect of contrast media in tumors on microangiography, suggestive of CA4P-induced tumor vascular shutdown, with the residual vessels only at the periphery (Fig. 2*G*, *I*, 5*G*, 5*I*).

Table 1. Characteristics of Primary and Secondary Liver Malignancies

Cellular Differentiation of Liver Malignant Tumors	Number of Lesions	Mean Tumor Diameter (mm)	Mean ΔT/L	Mean CA4P-Induced Necrosis (%)
Primary HCC (n = 36)				
Well differentiated (I)	6	11.02 ± 3.08	0.75 ± 0.18	79.54 ± 29.31
Moderately differentiated (II)	15	11.08 ± 3.58	0.62 ± 0.17	71.56 ± 26.61
Poorly differentiated (III)	14	12.28 ± 4	0.55 ± 0.16	48.40 ± 27.68
Undifferentiated (IV)	1 (angioma like)	9.09	0.04	0
Secondary liver tumor (n = 6)				
Undifferentiated (IV)	6	10.99 ± 4.42	0.43 ± 0.04	95.45 ± 6.97
Total	42	Mean ± SD 11.41 ± 3.67	0.58 ± 0.19	66.69 ± 31.18

Note: ΔT/L: change of tumor-to-liver contrast by Mn-DPDP enhanced MRI; CA4P: combretastatin A4-phosphate, SD: standard deviation.

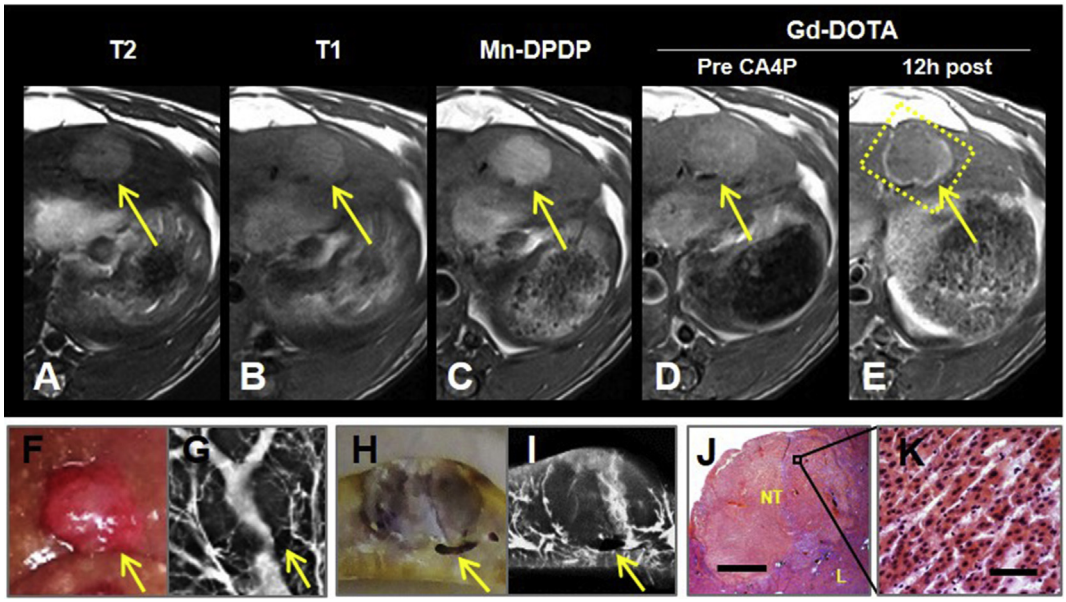

Figure 2. In vivo MRI and postmortem analyses of a representative grade I well-differentiated HCC before and after CA4P therapy. The HCC lesion (arrow) appeared mildly hyperintense both on T2WI (A) and T1WI (B). Twenty-four hours after Mn-DPDP injection, lesion conspicuity was greatly improved by the marked, homogeneous enhancement on T1WI (C). Two times of Gd-DOTA-enhanced T1WI revealed a mildly enhanced mass 4 h before CA4P treatment (D), and an unenhanced hypointense mass surrounded by an enhanced rim at 12 h after therapy (E), indicative of CA4P-induced massive tumor necrosis. Fresh specimen showed the CA4P-treated HCC on the surface of the left liver lobe (F). Gross microangiograph showed a less opaque mass superimposed by an opaque vascular trunk (G). Cross-section of the fixed tissue revealed the treated HCC with a clear boarder (H). The sectional microangiograph showed the tumor of largely barium sulfate filling defect with the cross of wide blood vessels (I). Low-power magnifying microscopy of H&E-stained slice (× 12.5 original magnification, scale bar = 800 μm. NT: necrotic tumor; VT: viable tumor; L: liver) depicted the tumor with above 90% CA4P-induced necrosis (J). High-power magnifying microscopy of H&E-stained slice (× 400 original magnification, scale bar = 25 μm) revealed a freshly necrotic grade I well-differentiated HCC as the tumor cells are arranged in an irregular thin trabecular pattern with pyknotic nuclei (K).

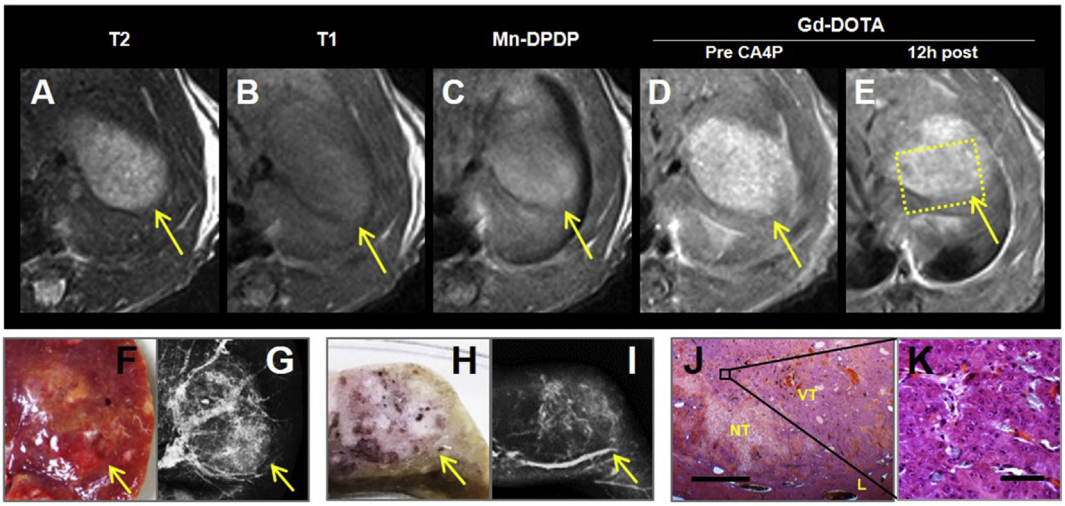

Figure 3. In vivo MRI and postmortem analyses of a representative grade II moderately differentiated HCC (arrow) before and after CA4P therapy. Before treatment, the mass looked hyerintense on T2WI (A) almost isointense on T1WI (B), mildly enhanced by Mn-DPDP on T1WI at 24 h (C), and markedly enhanced by Gd-DOTA on T1WI (D). Twelve hours after CA4P administration, only a patchy Gd-DOTA-enhanced lesion showed up, suggesting intratumoral focal necrosis (E). Grossly, the tumor was identified on the surface of left liver lobe (F) with inhomogeneous tumor opacification on gross microangiograph (G). The cutting surface of the fixed tumor section revealed scattered hemorrhage (H), corresponding to regionally sparser vasculature as shown on sectional microangiogram (I). H&E staining revealed only 46% CA4P-induced tumoral necrosis on low-power magnifying (× 12.5 original magnification, scale bar = 800 μm. NT: necrotic tumor; VT: viable tumor; L: liver) microscopy (J). Based on high-power magnifying microscopy (× 400 original magnification, scale bar = 25 μm), a grade II moderately differentiated HCC was classified based on the median trabecular pattern consisting about 4 layers of cancer cells (K).

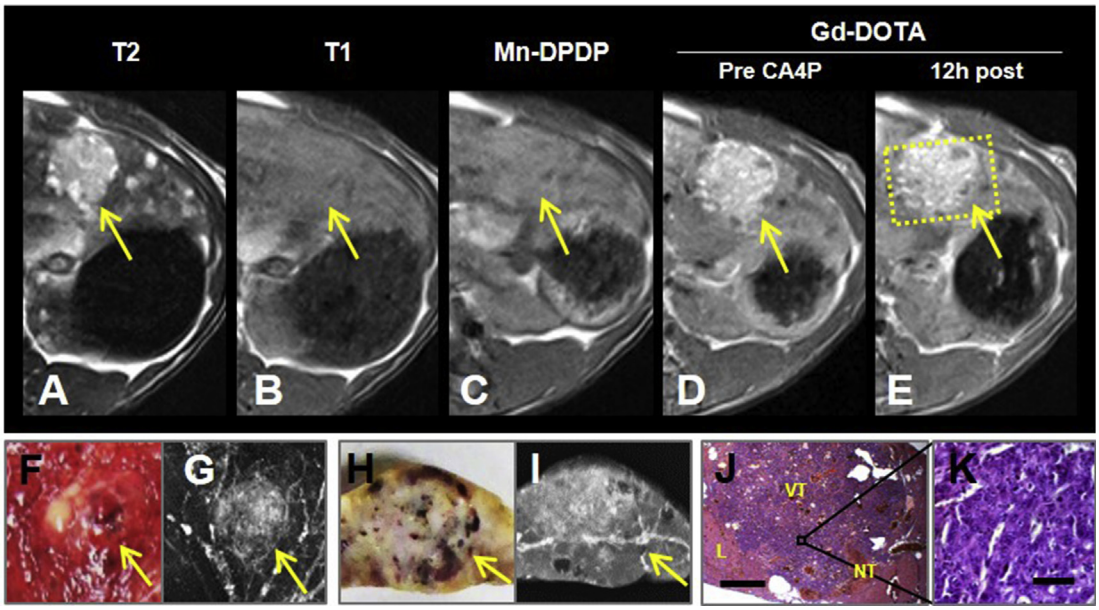

Figure 4. In vivo MRI and postmortem analyses of a representative grade III poorly differentiated HCC (arrow) before and after CA4P therapy. The lesion was inhomogeneously hyperintense on T2WI (A), but hardly visible on T1WI (B), and 24 h after Mn-DPDP-enhancement, the HCC lesion did not show any contrast uptake suggesting a loss of hepatocytic function (C). On Gd-DOTA-enhanced T1WIs, the lesion showed marked heterogeneous enhancement before treatment (D) but had hardly a change 12 h after CA4P therapy (E), indicative of a lack of tumor necrosis. Grossly, the lesion was seen on the surface of left liver lobe (F). The gross microangiograph showed a hypervascularized lesion (G). The cutting surface of the fixed tissue block revealed a well-defined mass with heterogeneous components (H). Sectional microangiograph (I) confirmed the gross finding (G). H&E-stained microscopy (× 12.5 original magnification, scale bar = 800 μm. NT: necrotic tumor; VT: viable tumor; L: liver) revealed only 20% CA4P-caused tumoral necrosis (J). A grade III poorly differentiated HCC was diagnosed by using high-power magnifying microscopy (× 400 original magnification, scale bar = 25 μm), displaying the broad-trabecular structure of cancer cells with higher nuclear irregularity, hyperchromatism, and nuclear-cytoplasmic ratio (K).

Histopathologically, coagulative and hemorrhagic necrosis could be identified on both the gross specimen (Figs. 2*H* and 5*H*) and H&E-stained slices (Fig. 2*J*, *K*, 5*J*) with little residual viable tumor tissue (Fig. 5*K*). In comparison, partial or focal necrosis in moderately (Fig. 3*J* and *K*) and poorly (Fig. 4*J* and *K*) differentiated HCCs was microangiographically featured by regional sparse tumor vasculature (Fig. 3*G*, *I*, 4*G*, 4*I*) and macroscopically verified on gross and sectional specimens (Fig. 3*F*, *H*, 4*F*, 4*H*).

Predicting Therapeutic Responses of HCCs to CA4P by Mn-DPDP-Enhanced MRI

As an example of intraindividual comparison, two HCCs of poor and moderate cellular differentiation developed simultaneously in the same rat at the same liver transection (Fig. 6). Before therapy, two HCCs appeared hyperintense and isointense on T2WI (Fig. 6*A*) and T1WI (Fig. 6*B*), respectively, they were persistently enhanced by Mn-DPDP (Fig. 6*C*). Based on the level of contrast uptake, the smaller HCCs with stronger contrast enhancement were suspected to be better differentiated from the larger ones. Accordingly, Gd-DOTA-T1WI at 12 h after CA4P treatment revealed more patchy unenhanced regions in the smaller lesion (Fig. 6*E*) in comparison with the pretreatment image (Fig. 6*D*). Eventually, these in vivo imaging findings were verified by postmortem examinations (Fig. 6*F*-*O*).

To further correlate cellular differentiation of HCCs with the change in tumor-to-liver contrast (ΔT/L) on Mn-DPDP-enhanced MRI and with CA4P-induced tumor necrosis, linear regressions were performed among the 36 primary HCCs and 6 secondary R1 liver tumors (Fig. 7*A* and *B*). Reverse correlation suggested that CA4P may induce greater tumor necrosis in highly differentiated HCCs (Fig. 7*A*), which was in line with the previous findings in a rat study of larger sample size without using a hepatobiliary CA [18]. Meanwhile, ΔT/L on Mn-DPDP-enhanced T1WI was also negatively correlated with HCC differentiation grade (Fig. 7*B*), indicative of the predictive value of in vivo delayed Mn-DPDP-enhanced MRI for HCC cellular differentiation and CA4P response. Quantitatively, well-differentiated HCCs exhibited a significantly higher ΔT/L by Mn-DPDP-enhanced MRI than that poorly differentiated HCCs did (Fig. 7*B*). Understandably, secondary R1 liver tumors displayed much lower ΔT/L than well- differentiated to poorly differentiated primary HCCs did (Fig. 7*B*). Owing to the considerable overlap of ΔT/L among primary HCCs in various differentiation grades and secondary liver tumors, a cutoff value was introduced to further investigate the predictive performance of ΔT/L on distinguishing various differentiation grades of HCCs and on identifying secondary liver tumors from primary HCCs. As shown in Table 2, a cutoff value of smaller than 0.487 mm^2/s was noted for distinction of secondary liver tumors ($P < 0.0001$) with the highest sensitivity (77%) and specificity (100%); but no significant threshold value of ΔT/L was obtained between the consecutive differentiation grades of primary HCCs.

Discussion

In this study, we have explored the predictive value of Mn-DPDP-enhanced MRI as a noninvasive surrogate to the invasive biopsy for making differential diagnosis among primary and secondary hepatic

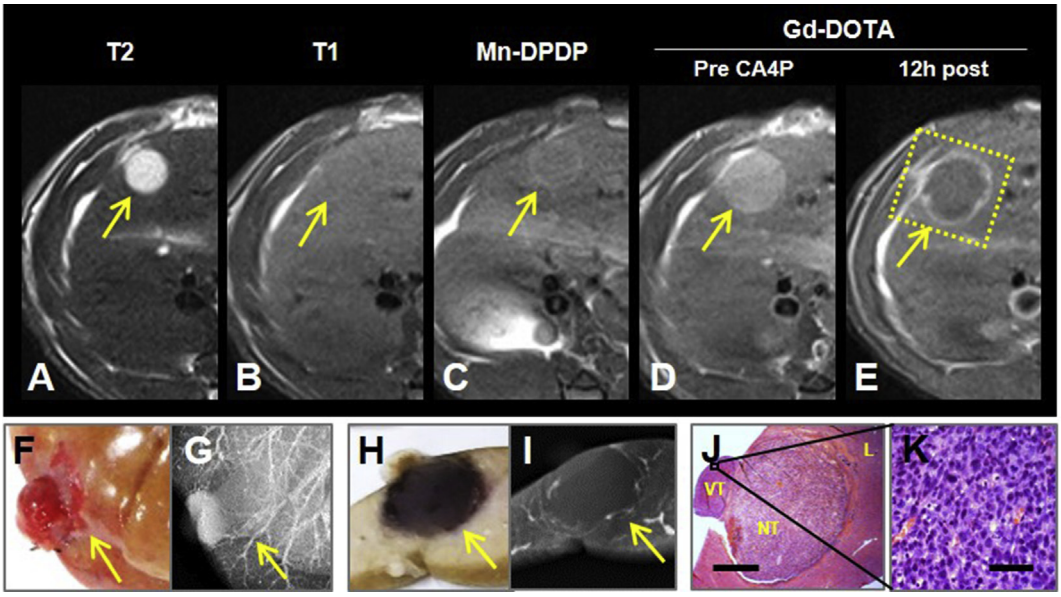

Figure 5. In vivo MRI and postmortem analyses of a representative secondary R1 liver tumor (arrow) before and after CA4P therapy. The nodule exhibited an extreme hyperintensity on T2WI (A), but faint isointensity on precontrast T1WI (B). Mn-DPDP depicted the lesion as a hyperenhanced rim peripheral to a central bulk of isointensity at 24 h, which classified the lesion as secondary liver tumor (C). On Gd-DOTA-enhanced T1WIs, initially the nodule was entirely and homogeneously enhanced (D); 12 h after CA4P treatment, only a thin peripheral enhancement was shown (E), demonstrating the remarkable tumoricidal effect. Grossly, a tumor was partially identified on the surface of the left liver lobe (F), which corresponded to a lesion with less contrast filling on gross microangiography but residual vasculature in the exophytic tumor extending to peritoneal cavity (G). The cutting surface of the fixed tissue block revealed brownish tumor of almost complete tumor necrosis with a part bulging on the liver surface, representing the remaining viable tumoral part in the free abdominal cavity (H). Sectional microangiograph (I) showed only little opacified peritumoral vasculature but absent vasculature in bulky tumor (I). Low-power magnifying H&E-stained microscopy (× 12.5 original magnification, scale bar = 800 μm. NT: necrotic tumor; VT: viable tumor; L: liver) revealed nearly complete CA4P-induced tumoral necrosis with only an exophytic portion of tumor that kept alive by ascites nourishment (J). The nodule was confirmed by high-power magnifying microscopy (× 400 original magnification, scale bar = 25 μm) as rhabdomyosarcoma based on the small, oval or round or spindle-like cancer cells with small amount of eosinophilic cytoplasm and hyperchromatic nuclei (K).

malignancies with varying grades of differentiation in rats and further for guiding the treatment of liver tumors with VDAs such as CA4P. Specifically, the change of tumor-to-liver contrast ($\Delta T/L$) derived from delayed Mn-DPDP enhancement was significantly greater in the HCCs with better differentiation than that in those of poorer differentiation, resulting in an inverse correlation between the $\Delta T/L$ and the histopathological grade of HCCs. Furthermore, the therapeutic efficacy of CA4P as expressed by the amount of induced tumor necrosis negatively correlated with HCC differentiation grade. In addition, comparing that with differentiated HCCs, $\Delta T/L$ was smaller in an undifferentiated HCC and secondary R1 liver tumors that often characterized with a peritumoral rim enhancement.

Mn-DPDP (Teslascan) is the only FDA-approved manganese CA for MRI and has been successfully used in the clinic for the diagnosis of nodular liver lesions. Actually, it has been proven to be a safe contrast media under the approved dose of 5−10 μmol/kg by a slow intravenous infusion over 15 min [27,28]. Nevertheless, Mn-DPDP has been withdrawn from the global markets in 2012 because of unsuccessful marketing and possible safety concerns. However, recently discovered nephrogenic systemic fibrosis and its association with gadolinium (Gd)-based MRI CAs have threatened the future use of lanthanide-based metals. Consequently, manganese-based agents are now regaining tremendous attentions [17].

Being a trace element essential to human health, the non-lanthanide paramagnetic metal manganese of bivalent state (Mn^{2+}) carries five unpaired electrons to provide efficient positive T1 signal contrast enhancement. However, excessive exposure to free Mn ions may cause systemic disorders or toxicity, which could be prevented by proper entropy using a chelator such as DPDP. Biochemically, Mn-DPDP was designed to be taken up by hepatocytes and eliminated via the biliary tract [13]. Actually, being a slow releaser of Mn^{2+}, Mn-DPDP dissociates in vivo into the Mn^{2+} and DPDP, where the Mn^{2+} is absorbed by hepatocytes via membrane calcium channels and excreted into the bile, whereas the DPDP is eliminated into urine through the renal filtration. Although Mn-DPDP is not free from toxicity, it evidently offers a potent MRI CA. Besides, the safety factor (LD50/effective dose) of Mn-DPDP is 540, much higher than the safety factor (60−100) of the first commercial linear MRI CA gadolinium diethylenetriaminepentaacetic acid (Gd-DTPA) [29].

Previously, most of the publications regarding the applications of Mn-DPDP-enhanced MRI in the liver addressed the maximum liver parenchymal enhancement occurring at 15 min onward until a few hours after contrast administration, where contrast-to-noise ratio between liver parenchyma and nonhepatocellular nodular lesions reached five-fold higher than that on precontrast images [29]. Delayed enhancement overnight after Mn-DPDP intravenous administration is also of unique value for characterizing primary HCCs of a full spectrum of differentiation and metastatic lesions from extrahepatic origins [11−15]. Consistently, in this study, a high $\Delta T/L$ on delayed enhancement MRI at 24 h among grade I-III HCCs

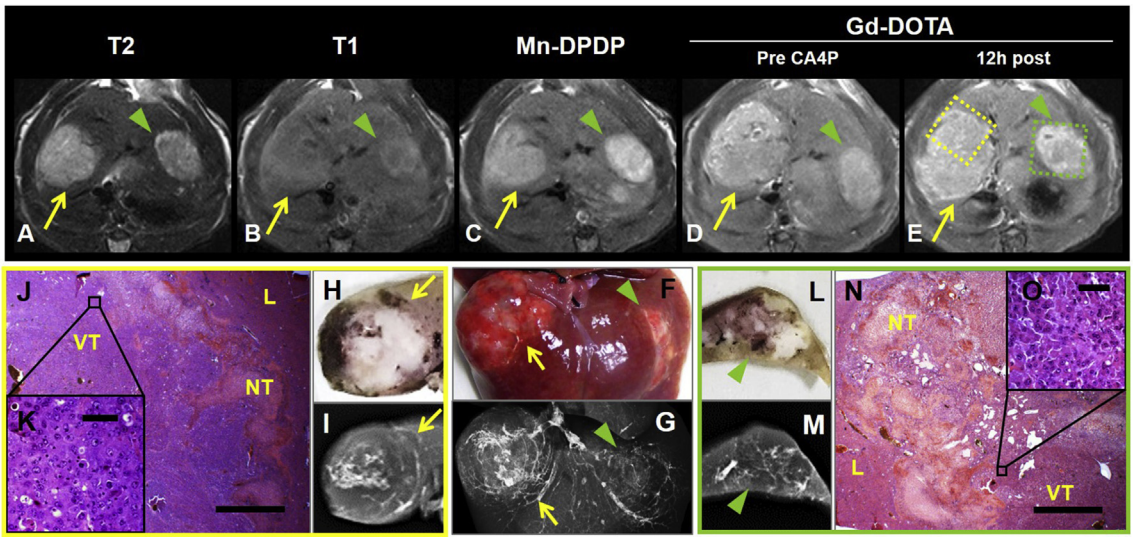

Figure 6. In vivo MRI and postmortem analyses of 2 HCCs with poor (arrow) and moderate (arrowhead) differentiation in response to CA4P treatment on the same cross-section for intraindividual comparison. Both lesions appeared hyperintense on T2WI (A), isointense to slightly hyperintense on precontrast T1WIs (B). On Mn-DPDP-enhanced 24-h-delayed image, the larger lesion (arrow) in the median lobe was moderately enhanced, whereas the smaller lesion (arrowhead) in the left lobe appeared strongly enhanced, suggesting different levels of residual hepatocytic function (C). On Gd-DOTA-enhanced T1WIs, both tumors were nonspecifically enhanced before treatment (D). But 12 h after CA4P administration, both lesions were also positively enhanced with patchy and regional loss of enhancement more obvious in the smaller lesion (arrowhead), suggesting certain CA4P-induced necrosis (E). Grossly, both the larger (arrow) and smaller (arrow head) HCC lesions were identified on the surface of the median and left liver lobes, respectively (F). The cutting surface of the fixed tumor specimens confirmed the presence of these two HCC lesions (H, L) with the smaller one demonstrating partial hemorrhagic tumor necrosis (L). Gross (G) and sectional (I, M) microangiographs showed more residual tumoral vasculature in the larger lesion (arrow) compared to the small one (arrowhead). Low-power magnifying microscopies (× 12.5 original magnification, scale bar = 800 μm. NT: necrotic tumor; VT: viable tumor; L: liver) of H&E-stained slides revealed CA4P induced 28% and 63% tumoral necrosis, respectively, in the larger (J) and smaller (N) lesions. On high-power magnifying microscopies (× 400 original magnification, scale bar = 25 μm), the larger tumor was classified as a grade III poorly differentiated HCC due to the solid pattern, giant cells and bizarre nuclei (K), whereas the smaller one was identified as a Grade moderately differentiated HCC based on the trabecular pattern of cancer cells (O).

could be attributed to the abundant Mn^{2+} retention in differentiated hepatoma cells, whereas a low ΔT/L found typically in the grade IV HCC and secondary R1 tumors was likely due to the dysfunction of Mn^{2+} uptake in malignant cells without hepatocytic differentiation.

In spite of statistical significances, there was a considerable overlap of ΔT/L among HCCs of different histological grades, which is in line with the previous study outcomes about Mn-DPDP [11–15,30]. Such a prolonged Mn-DPDP enhancement renders a wide time window for

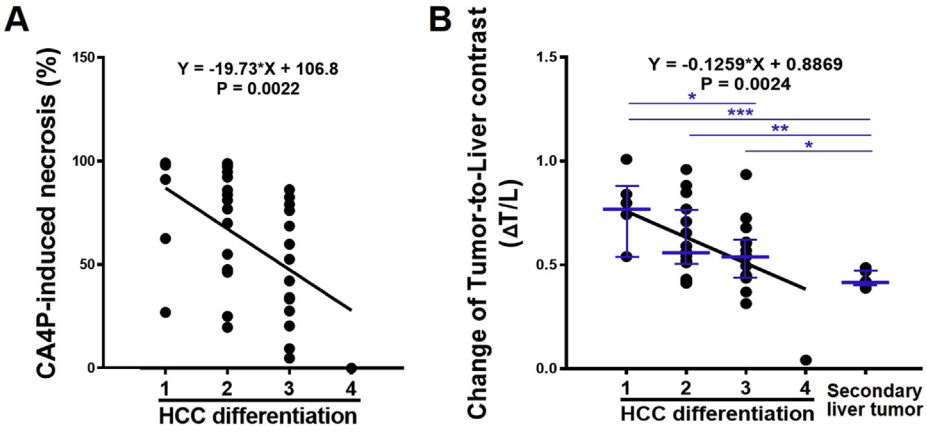

Figure 7. Correlations of the HCC differentiation with CA4P-induced tumoral necrosis and with Δ T/L on Mn-DPDP-enhanced image. (A) Percentile CA4P-induced tumor necrosis quantified by histopathology was negatively correlated (**$P < 0.01$) with HCC differentiation. (B) ΔT/L (change of tumor-to-liver contrast) derived at 24 h from Mn-DPDP-enhanced MRI showed a significantly negative correlation (**$P < 0.01$) with cellular differentiation of HCCs. ΔT/L was compared by the Kruskal–Wallis test in-between primary HCCs of a full spectrum of cellular differentiation and the secondary R1 tumors, in which data were presented as the median ± interquartile range (IQR). A significant difference was seen between grade I and grade III HCCs (*$P < 0.05$) and between implanted R1 tumors and grade I HCCs (***$P < 0.001$), grade II HCCs (**$P < 0.01$), as well as grade III (*$P < 0.05$).

Table 2. Cutoff Values of $\Delta T/L$ and the Corresponding Sensitivity and Specificity in Differentiating Hepatic Malignancies

	Cutoff Values of ΔT/L ($\times 10^{-2}$ mm^2/s)	Sensitivity (95% CI)	Specificity (95% CI)	*P* value
Well-differentiated from moderately differentiated HCCs	≥70.9	73.3 (44.9−92.2)	66.7 (22.3−95.7)	0.1797
Moderately from poorly differentiated HCCs	≥49.4	42.9 (17.7−71.1)	80 (51.9−95.7)	0.3588
Poorly differentiated HCCs from secondary liver tumors	≥48.7	100 (54.1−100)	64.3 (35.1−87.2)	0.0073**
Primary HCCs in all differentiation grades from secondary liver tumors	≥48.7	100 (54.1−100)	77.1 (59.9−89.6)	<0.0001***

Note: CI: confidence interval.
**$P < 0.01$; ***$P < 0.001$.

more accurately scanning and discriminating intrahepatic nodular lesions [31]. The observed peritumoral rim enhancement can be considered resulting from outward infiltration of malignant cells that sequester normal hepatocytes and hinder their biliary Mn^{2+} excretion [13,30]. Our results demonstrated that indeed Mn-DPDP-enhanced MRI at 24 h raised the sensitivity of rim enhancement in depicting secondary R1 liver tumors. Similarly, both animal and clinical studies [13,14] revealed more reliable and significant rim and segmental enhancements by Mn-DPDP on 24-h delayed MRI. In fact, compared with early imaging at 30 min after Mn-DPDP administration, MRI at 24 h could greatly increase the sensitivity of rim enhancement after washout of the CA from liver parenchyma [14].

The VDAs including CA4P target the abnormal endothelial cells of the tumoral vasculature rather than the malignant tumor cells such as HCCs on which Mn-DPDP-enhanced MRI may help to characterize their cellular differentiation or their degree of malignancy. The reasons why Mn-DPDP-enhanced MRI may predict, to certain extent, the therapeutic efficacy of VDAs on HCCs are understandable. Previous study indicates that 1) the degree of vascularity positively correlates with the cellular differentiation grade, i.e., well-differentiated grade I HCCs are less vascularized than the undifferentiated grade IV HCCs [11−15,30] and 2) CA4P could induce greater tumor necrosis among lower grade I-II HCCs as compared with that in those higher grade III-IV HCCs [18]. This study proved that indeed HCCs with more Mn-DPDP retention showed greater CA4P-induced tumor necrosis. These better differentiated HCCs usually contain thinner abnormal blood vessels that are more vulnerable to VDA attack leading to more extensive vascular shutdown and consequent tumor ischemic necrosis. Paradoxically, metastatic or secondary liver tumors such as R1 allografts in this study are almost all high-grade malignancies, but they often exhibit nearly complete tumor necrosis after VDA treatment [18,30,32,33]. This can be explained by the fact that these metastatic tumors are not native to the liver and do not tend to develop tumor blood vessels with wider diameters that could help to escape the VDA attack. The detailed mechanisms therein have to be elucidated by further experimental studies.

Over the past decades, global multicenter clinical trials on the VDA alone or in combination with other anticancer drugs have been conducted, but none of the VDAs have been approved by the FDA because of their inadequate efficacy to eradicate all malignant cells and limited patient survival [34]. To overcome the leftover tumor residues as a bottleneck problem of all VDAs, a novel dual targeting pan-anticancer theragnostic strategy namely OncoCiDia has been developed [19,20] where the second necrosis-targeting radiotherapy relies on the maximized tumor necrosis caused by the first attack of a VDA such as CA4P. In rats, CA4P exerted diverse tumoricidal efficacy in primary HCCs with heterogeneous histomorphology [18,35] and demonstrated a reverse correlation with HCC's cellular differentiation in this study. Therefore, proper patient selection is critical to maximize the efficacy of OncoCiDia on HCCs.

In this context, Mn-DPDP-enhanced MRI as a noninvasive predictor of CA4P-induced necrosis in primary and secondary liver cancers may play a crucial role in patient selection for clinical application of OncoCiDia for the treatment of HCCs. If this could be proven by future clinical trials, the translational value of this study to help revive both the diagnostic Mn-DPDP and therapeutic VDAs in clinical oncology can be realized. Clinically, if Mn-DPDP-enhanced MRI implies an unlikely response of patient's HCC lesion to VDA treatment, minimally invasive alternatives such as radiofrequency ablation and microwave can be adopted to necrotize the tumor.

In conclusion, Mn-DPDP-enhanced MRI at a 24-h delayed phase shows promise as an imaging biomarker for estimating histological differentiation of HCCs and for distinguishing secondary liver tumors, thereby predicting the therapeutic efficacy of VDAs for the treatment of primary and secondary liver cancers. These findings may facilitate noninvasive patient selection for the initial clinical trials of VDA-involved new therapies in patients with HCCs of a full differentiation spectrum. Meanwhile, this study may contribute to the reflourishing usage of Mn-based MRI CAs by endowing their role in guidance of clinical interventions for hepatic malignancies as a new indication.

Declarations of interest

None.

Acknowledgments

This work has partially been supported by KU Leuven projects IOF-HB/08/009 and IOF-HB/12/018; the KU Leuven Molecular Small Animal Imaging Center MoSAIC (KUL EF/05/08); European Union (Asia-Link CfP 2006-EuropeAid/123738/ACT/Multi-Proposal No. 128−498/111); the National Natural Science Foundation of China (Grant No. 81603142, 81830052, 81530053, 81471685); Construction project of Shanghai Key Laboratory of Molecular Imaging (18DZ2260400); Shanghai Municipal Education Commission (Class II Plateau Disciplinary Construction Program of Medical Technology of SUMHS, 2018−2020); and by research grants from "973" Project (2012CB932604), New Drug Discovery Project (2012ZX09506-001-005. Liu YW is sponsored by a scholarship from the Center of Excellence In Vivo Molecular Imaging Research (IMIR). The corresponding author Yicheng Ni was a Bayer Lecture Chair holder.

References

[1] Seale MK, Catalano OA, Saini S, Hahn PF and Sahani DV (2009). Hepatobiliary-specific MR contrast agents: role in imaging the liver and biliary tree. *RadioGraphics* **29**, 1725−1748.

[2] Lohrke J, Frenzel T and Endrikat J, et al (2016). 25 Years of contrast-enhanced MRI: developments, current challenges and future perspectives. *Adv Ther* **33**, 1−28.

[3] Oudkerk M, Torres CG and Song B, et al (2002). Characterization of liver lesions with mangafodipir trisodium-enhanced MR imaging: multicenter study comparing MR and dual-phase spiral CT. *Radiology* **223**, 517–524.
[4] Scharitzer M, Schima W and Schober E, et al (2005). Characterization of hepatocellular tumors: value of mangafodipir-enhanced magnetic resonance imaging. *J Comput Assist Tomogr* **29**, 181–190.
[5] Huppertz A, Balzer T and Blakeborough A, et al (2004). Improved detection of focal liver lesions at MR imaging: multicenter comparison of gadoxetic acid-enhanced MR images with intraoperative findings. *Radiology* **230**, 266–275.
[6] Marchal G, Zhang X, Ni Y, Van Hecke P, Yu J and Baert AL (1993). Comparison between Gd-DTPA, Gd-EOB-DTPA, and Mn-DPDP in induced HCC in rats: a correlation study of MR imaging, microangiography, and histology. *Magn Reson Imaging* **11**, 665–674.
[7] Ni Y, Marchal G and Vandamme B, et al (1992). Magnetic resonance imaging, microangiography, and histology in a rat model of primary liver-cancer. *Investig Radiol* **27**, 689–697.
[8] Ni Y, Marchal G, Yu J, Mühler A, Lukito G and Baert AL (1994). Prolonged positive contrast enhancement with Gd-EOB-DTPA in experimental liver tumors: potential value in tissue characterization. *J Magn Reson Imaging* **4**, 355–363.
[9] Jaw TS, Chen SH and Wang YM, et al (2012). Comparison of Gd-Bz-TTDA, Gd-EOB-DTPA, and Gd-BOPTA for dynamic MR imaging of the liver in rat models. *Kaohsiung J Med Sci* **28**, 130–137.
[10] Fischbach F, Lohfink K and Gaffke G, et al (2013). Magnetic resonance-guided freehand radiofrequency ablation of malignant liver lesions: a new simplified and time-efficient approach using an interactive open magnetic resonance scan platform and hepatocyte-specific contrast agent. *Investig Radiol* **48**, 422–428.
[11] Ni Y, Marchal G and Zhang X, et al (1993). The uptake of manganese dipyridoxal-diphosphate by chemically induced hepatocellular carcinoma in rats. A correlation between contrast-media-enhanced magnetic resonance imaging, tumor differentiation, and vascularization. *Investig Radiol* **28**, 520–528.
[12] Murakami T, Baron RL and Peterson MS, et al (1996). Hepatocellular carcinoma: MR imaging with mangafodipir trisodium (Mn-DPDP). *Radiology* **200**, 69–77.
[13] Ni Y, Marchal G and Yu J, et al (1993). Experimental liver cancers: Mn-DPDP-enhanced rims in MR-microangiographic-histologic correlation study. *Radiology* **188**, 45–51.
[14] Koh DM, Brown G, Meer Z, Norman AR and Husband JE (2007). Diagnostic accuracy of rim and segmental MRI enhancement of colorectal hepatic metastasis after administration of mangafodipir trisodium. *Am J Roentgenol* **188**, W154–W161.
[15] Ni Y and Marchal G (1998). Enhanced magnetic resonance imaging for tissue characterization of liver abnormalities with hepatobiliary contrast agents: an overview of preclinical animal experiments. *Top Magn Reson Imaging* **9**, 183.
[16] Miller CG, Krasnow J and Schwartz LH (2014). Medical imaging in clinical trials. Springer Science & Business Media; 2014.
[17] Karlsson JOG, Ignarro LJ, Lundström I, Jynge P and Almén T (2015). Calmangafodipir [Ca4Mn(DPDP)5], mangafodipir (MnDPDP) and MnPLED with special reference to their SOD mimetic and therapeutic properties. *Drug Discov Today* **20**, 411–421.
[18] Liu Y, Keyzer FD and Wang Y, et al (2018). The first study on therapeutic efficacies of a vascular disrupting agent CA4P among primary hepatocellular carcinomas with a full spectrum of differentiation and vascularity: correlation of MRI-microangiography-histopathology in rats. *Int J Cancer* **143**, 1817–1828.
[19] Ni Yicheng (2014). Oncocidia: a small molecule dual targeting pan-anticancer theragnostic strategy. *Cancer Res* **74**, 1767.
[20] Li J, Sun Z and Zhang J, et al (2011). A dual-targeting anticancer approach: soil and seed principle. *Radiology* **260**, 799–807.
[21] Liu Y, Yin T and Feng Y, et al (2015). Mammalian models of chemically induced primary malignancies exploitable for imaging-based preclinical theragnostic research. *Quant Imaging Med Surg* **5**, 708–729.
[22] Liu YW, De Keyzer F and Feng YB, et al (2018). Intra-individual comparison of therapeutic responses to vascular disrupting agent CA4P between rodent primary and secondary liver cancers. *World J Gastroenterol* **24**, 2710–2721.
[23] Schlageter M, Terracciano LM, D'Angelo S and Sorrentino P (2014). Histopathology of hepatocellular carcinoma. *World J Gastroenterol* **20**, 15955–15964.
[24] World Health Organization, International Agency for Research on Cancer. In: Aaltonen LA, Hamilton SR, editors. Pathology and genetics of tumours of the digestive system. Lyon: Oxford: IARC Press: Oxford University Press (distributor); 2000.
[25] Kojiro M (2006). Pathology of hepatocellular carcinoma. Oxford: John Wiley & Sons, Ltd; 2006.
[26] Buijs M, Vossen JA and Geschwind JF, et al (2011). Quantitative proton MR spectroscopy as a biomarker of tumor necrosis in the rabbit VX2 liver tumor. *J Vasc Interv Radiol JVIR* **22**, 1175–1180.
[27] Torres CG, Lundby B and Sterud AT, et al (1997). MnDPDP for MR imaging of the liver. Results from the European phase III studies. *Acta Radiol Stockh Swed 1987* **38**, 631–637.
[28] Thomsen HS. In: Contrast media: safety issues and ESUR guidelines. Springer Science & Business Media; 2014. Book chapter Yuspa SH, Hennings H, Roop D, Strickland J, Greenhalgh DA. Genes and mechanisms involved in malignant conversion. In: Harris CC, Liotta LA, editors. Genetic mechanisms in carcinogenesis and tumor progression. New York: Wiley-Liss; 1990. pp.115–126.
[29] Elizondo G, Fretz CJ and Stark DD, et al (1991). Preclinical evaluation of MnDPDP: new paramagnetic hepatobiliary contrast agent for MR imaging. *Radiology* **178**, 73–78.
[30] Ni Y, Wang H and Chen F, et al (2009). Tumor models and specific contrast agents for small animal imaging in oncology. *Methods* **48**, 125–138.
[31] Rofsky NM and Earls JP (1996). Mangafodipir trisodium injection (Mn-DPDP). A contrast agent for abdominal MR imaging. *Magn Reson Imag Clin N Am* **4**, 73–85.
[32] Wang H, Sun X and Chen F, et al (2009). Treatment of rodent liver tumor with combretastatin a4 phosphate: noninvasive therapeutic evaluation using multiparametric magnetic resonance imaging in correlation with microangiography and histology. *Investig Radiol* **44**, 44–53.
[33] Wang H, Van de Putte M, Chen F, De Keyzer F, Jin L and Yu J, et al (2008). Murine liver implantation of radiation-induced fibrosarcoma: characterization with MR imaging, microangiography and histopathology. *Eur Radiol* **18**, 1422–1430.
[34] Tozer GM, Kanthou C, Lewis G, Prise VE, Vojnovic B and Hill SA (2008). Tumour vascular disrupting agents: combating treatment resistance. *Br J Radiol* **81**, S12–S20.
[35] Liu Y, Yin T and Keyzer F, et al (2017). Micro-HCCs in rats with liver cirrhosis: paradoxical targeting effects with vascular disrupting agent CA4P. *Oncotarget* **8**, 55204–55215.